nature materials

Article

https://doi.org/10.1038/s41563-025-02180-3

Terahertz photocurrent probe of quantum geometry and interactions in magic-angle twisted bilayer graphene

Received: 24 April 2024

Accepted: 18 February 2025

Published online: 24 March 2025

Check for updates

Roshan Krishna Kumar[1,2] ✉, Geng Li[1,19], Riccardo Bertini[1,19], Swati Chaudhary[3,4,19], Krystian Nowakowski[1], Jeong Min Park[4], Sebastian Castilla[1], Zhen Zhan[5], Pierre A. Pantaleón[5], Hitesh Agarwal[1], Sergi Batlle-Porro[1], Eike Icking[6,7], Matteo Ceccanti[1], Antoine Reserbat-Plantey[1,8], Giulia Piccinini[1], Julien Barrier[1], Ekaterina Khestanova[1], Takashi Taniguchi[9], Kenji Watanabe[10], Christoph Stampfer[6,7], Gil Refael[11], Francisco Guinea[5,12], Pablo Jarillo-Herrero[4], Justin C. W. Song[13], Petr Stepanov[1,14,15], Cyprian Lewandowski[11,16,17] & Frank H. L. Koppens[1,18] ✉

Moiré materials represent strongly interacting electron systems bridging topological and correlated physics. Despite notable advances, decoding wavefunction properties underlying the quantum geometry remains challenging. Here we utilize polarization-resolved photocurrent measurements to probe magic-angle twisted bilayer graphene, leveraging its sensitivity to the Berry connection that encompasses quantum 'textures' of electron wavefunctions. Using terahertz light resonant with optical transitions of its flat bands, we observe bulk photocurrents driven by broken symmetries and reveal the interplay between electron interactions and quantum geometry. We observe inversion-breaking gapped states undetectable through quantum transport, sharp changes in the polarization axes caused by interaction-induced band renormalization and recurring photocurrent patterns at integer filling factors of the moiré unit cell that track the evolution of quantum geometry through the cascade of phase transitions. The large and tunable terahertz response intrinsic to flat-band systems offers direct insights into the quantum geometry of interacting electrons and paves the way for innovative terahertz quantum technologies.

Twisted bilayer graphene (TBG) represents a new paradigm for exploring the interplay of strongly interacting phenomena[1–3] with non-trivial topology[4–6]. Although previous experiments have revealed several exotic correlated and topological phenomena[7], the measurements of quantum geometry remain challenging, relying on the observation of broken-symmetry phases driven by electron–electron interactions[4–6] that occur only at specific band filling. Furthermore, the underlying symmetries driving such phenomena are often local[8,9] because of their sensitivity to substrates[10], strain[11] and reconstruction[12], making them easily smeared in global measurements. Photocurrent measurements provide a powerful complementary probe to study quantum materials[13]. The bulk photovoltaic effect (BPE)[14,15] represents an intriguing class of photocurrent phenomena in which the current is generated by broken symmetries intrinsic to the crystal. Aside from its promise for photovoltaics[16], it has gained notable attention for studying quantum materials because of its ties to the second-order conductivity, $\sigma_{abc}\,(a,b,c = x,y,z)$, whose magnitude is controlled by the geometric

A full list of affiliations appears at the end of the paper. ✉e-mail: roshan.krishnakumar@icfo.eu; frank.koppens@icfo.eu

https://doi.org/10.1038/s41563-025-02180-3

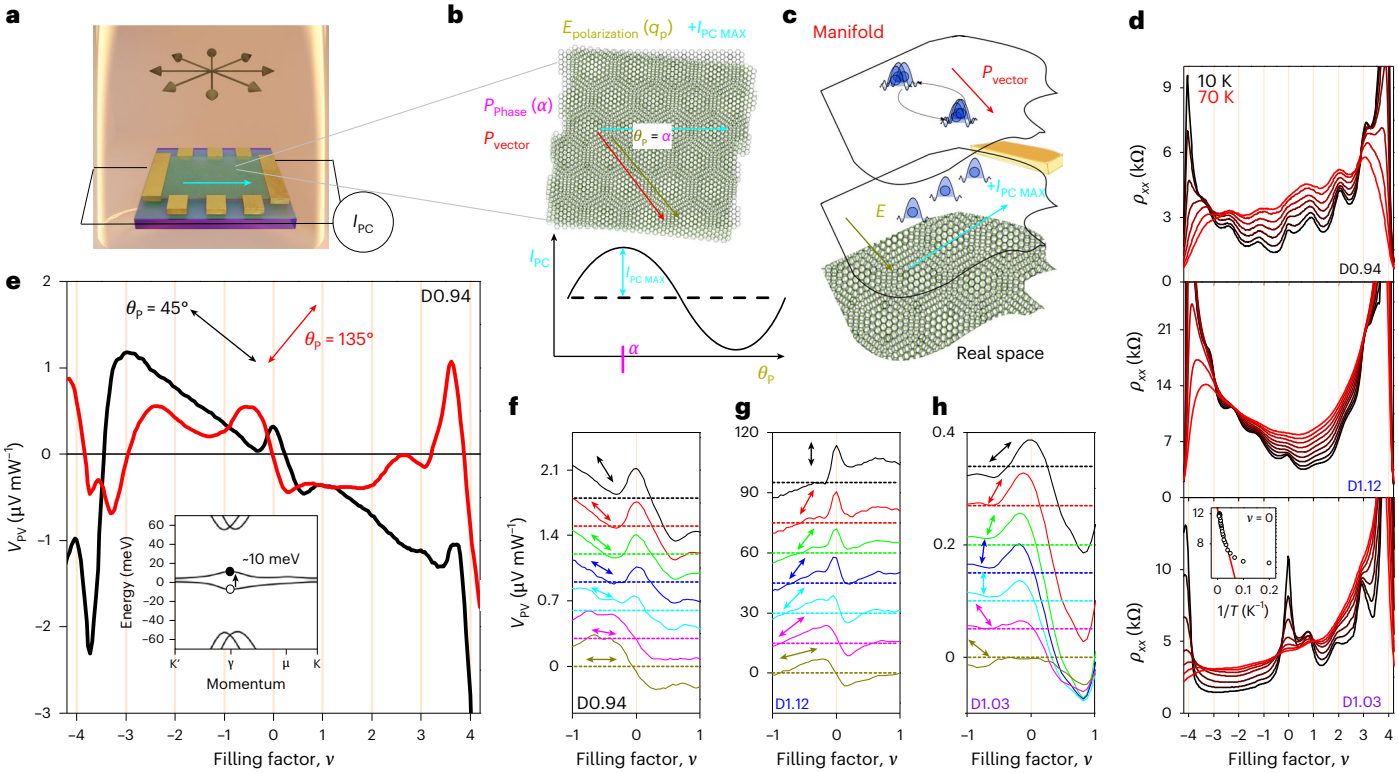

Fig. 1 | Polarization-dependent THz photocurrents in TBG. a, Schematic of THz photocurrent experiments. The yellow arrows indicate the polarization of light. The solid cyan arrows indicate the projection of the generated photocurrent along the measurement contacts (I_{PC}). **b**, Top: schematic of the underlying TBG (grey) on hBN (green). The cyan, red and dark yellow arrows depict I_{PC}, the polarization vector intrinsic to quantum geometry and θ_P of the incident electric field, respectively. When the polarization of light is aligned with the polarization vector, the photocurrent is maximum. The polarization vector forms an angle with the current projection called the polarization phase (α). Bottom: $I_{PC}(\theta_P)$ is sinusoidal with a maximum at $\theta_P = \alpha$. **c**, Schematic of the quantum geometric response. The top slice depicts electrons transitioning between quantum states driven by the optical field. Electric-field alignment with the polarization vector drives an anomalous current response (middle slice). **d**, Resistivity (ρ_{xx}) as a function of ν plotted for different temperatures in D0.94, D1.12 and D1.03. Bottom (inset): $\rho_{xx}(T)$ for $\nu = 0$ (open circles). The red dashed line plots an exponential fit from which gaps of 3.6 meV are extracted. **e**, V_{PV} as a function of ν, plotted for two orthogonal polarizations of THz light (black and red curves). Inset: band structure of magic-angle TBG with THz transitions. **f**, Zoomed-in data of V_{PV} close to the CNP for different polarization directions. The solid lines are experimental data offset for clarity and the dashed lines indicate the $V_{PV} = 0$ line. **g**,**h**, Same data as **f** for D1.12 (**g**) and D1.03 (**h**). Data from D1.12 were obtained at 0.7 THz (2.7-meV excitation) whereas all other datasets were obtained at 2.5 THz (10 meV).

properties of electron wavefunctions and the projection of electric field (E) relative to the crystal lattice $J_c = \sigma_{abc}E_aE_b$. Moreover, even if photoexcitation is global, local photoactive regions of interest may still be discerned, making the BPE a potentially more sensitive probe of electronic orders.

Polarization-dependent measurements allow to rotate E arbitrarily (Fig. 1a), which serves as a powerful tool for probing quantum geometry and underlying symmetries of the system. The polarization phase (α) and the polarization angle (θ_P) relative to contacts in which the current is maximum (Fig. 1b) describe an intrinsic quantum direction manifested by geometric phases accumulated when electrons transition within (intraband) or between (interband) manifolds of quantum states (Fig. 1c). Although distinct microscopic mechanisms exist coupled to different physical quantities[13], for example, the Berry curvature or shift vector, all of them are built from various gauge-invariant combinations of Berry connections, which capture changes in the internal structure of electron wavefunctions between two quantum mechanical states coupled by optical fields. Therefore, in moiré materials, second-order conductivities are anticipated to be extraordinarily large[17–21] because their giant superlattice unit cell (~10 nm) sets the scale of the Berry connection[22]. Moreover, they can be particularly strong at terahertz (THz) frequencies because of the large joint density of states resonant at millielectronvolt (meV) energy scales inherent to flat bands[19,20] (Fig. 1e, inset). Here we report a large and polarization-sensitive THz photoresponse in magic-angle TBG and use it to study the interplay between electron interactions and quantum geometry at the energy scale of its flat bands. Specifically, we probe the quantum geometric textures of the gapped state at charge neutrality[23], electron–electron-interaction-induced band renormalizations[24] and cascade phenomena[25,26].

Results

We studied four devices close to the magic angle, with twist angles of 0.94°, 1.02°, 1.03° and 1.12°, denoted as D0.94, D1.02, D1.03 and D1.12, respectively (Methods provides the fabrication details). All devices showed oscillating features in the resistivity around an integer filling factor (ν) at 10 K, which we attribute to the parent states of correlated phenomena (Fig. 1d and Supplementary Fig. 8a), and low twist-angle inhomogeneity verified through multiterminal quantum transport measurements[27]. However, their behaviour differs at the charge neutrality point (CNP). D0.94 and D1.12 showed a monotonic increase in resistivity with temperature, indicating metallic behaviour, whereas D1.03 exhibits a marked insulating peak showing activation behaviour on increasing temperature (Fig. 1d, inset). This behaviour indicates gapping of the flat bands, as expected for TBG aligned to hexagonal boron nitride (hBN)[10]. The gap serves as a signature of broken $C_{2z}T$ symmetry, where C_{2z} denotes a two-fold rotation about the z axis and T indicates time reversal, which is a prerequisite for driving in-plane

https://doi.org/10.1038/s41563-025-02180-3

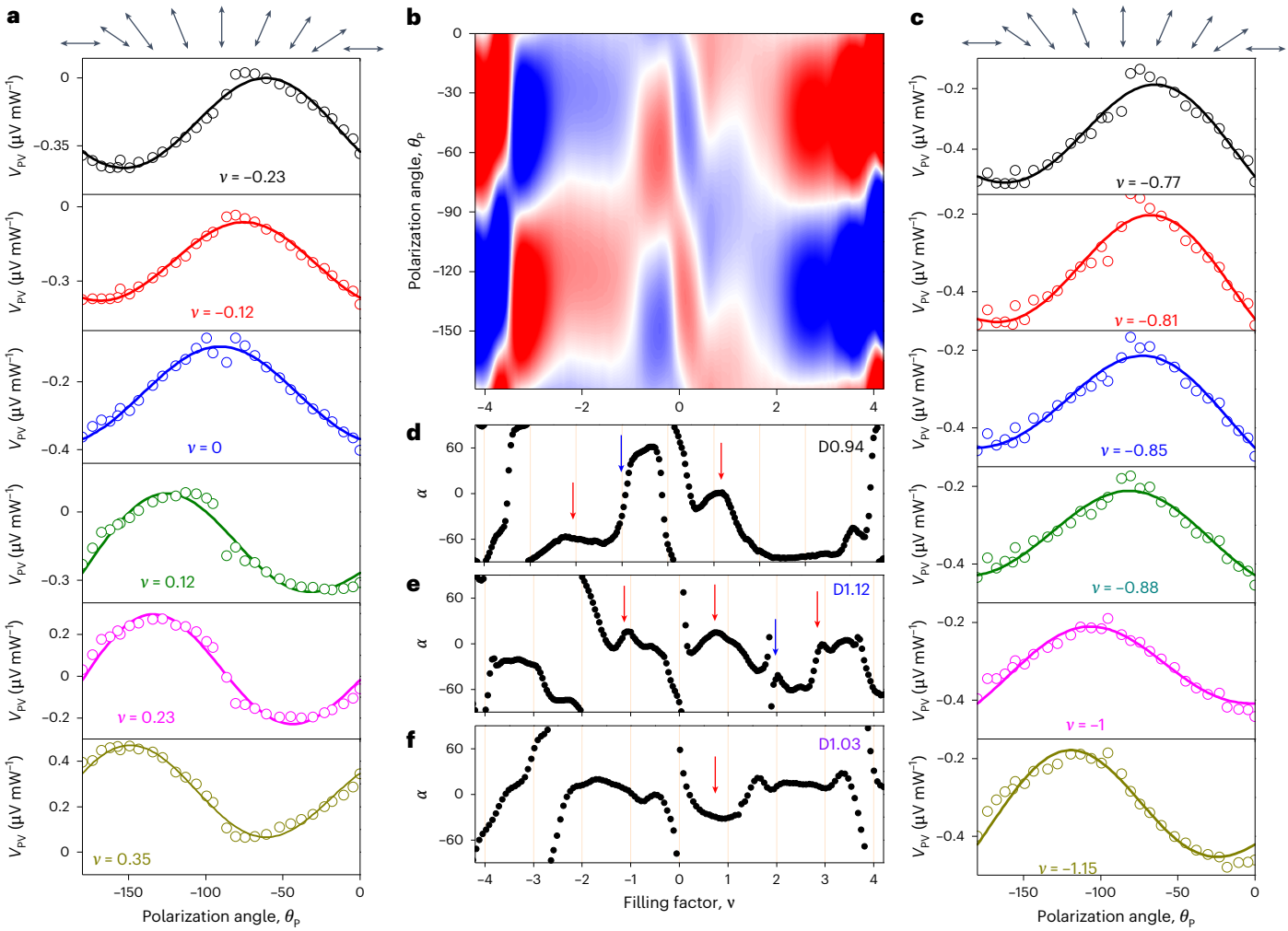

Fig. 2 | ν dependence of α in TBG. a, V_{PV} measured as a function of θ_P for different ν values (top to bottom) in D0.94. The open circles denote the experimental data and the solid lines plot the fits to equation (1). **b**, V_{Lin} as a function of ν and θ_p. Colour scale, blue (−0.5 μV mW^{-1}); red (0.5 μV mW^{-1}). **c**, Same data as **a**, but for filing close to ν = −1. **d**, α as a function of ν for D0.94 extracted from **b**. **e**,**f**, Same data as **d**, but for D1.12 (**e**) and D1.03 (**f**). The red and blue arrows in **d**–**f** highlight integer-ν features.

bulk photocurrents[14]. Nonetheless, in all our devices, we observed a strong bulk THz photoresponse that is polarization dependent, with similar characteristics as discussed below.

Polarization-resolved THz photocurrent measurements

Figure 1e displays the photovoltage (V_{PV}) as a function of ν measured in D0.94 for two orthogonal polarizations normalized by the incident power. We measure the photovoltage throughout this work; however, we find that the same behaviours could be observed also in the photocurrent. We find that the photoresponse for the two directions is strikingly different. The response differs not only in magnitude but the ν dependence also changes dramatically, even changing sign. The functional form also contrasts greatly with the photothermoelectric effect[28] (Supplementary Section 1), pointing towards a distinct origin. Of particular relevance is the behaviour around the CNP, which exhibits a peak for one polarization and zero-crossing behaviour for the other. Figure 1f details this behaviour, showing the peaked response evolving smoothly from the sign-changing response with polarization. Similar behaviours were observed for D1.12 (Fig. 1g) and D1.03 (Fig. 1h). Supplementary Section 2 shows the full dependence. D1.12 required smaller excitation energies to reveal such behaviour (Supplementary Section 3); we attribute this to the excitation energy approaching the inter-flat-band resonances of magic-angle TBG (Fig. 1e, inset). Figure 1 shows that the photoresponse around the CNP is very sensitive to polarization.

Figure 2a plots the full polarization-dependent response $V_{PV}(\theta_p)$ for different ν values close to the CNP. For all ν, we observe an oscillating photoresponse, indicating that the effect originates from light polarization (Supplementary Section 4 provides additional checks). In particular, we find that α is highly sensitive to ν. This behaviour contrasts with usual junction phenomena[28], device geometry[29] and antenna[30,31] effects, where α would be ν independent (Supplementary Section 5). Hence, the ν dependence underscores that the photocurrents and their polarization dependence are primarily governed by the electronic system.

To further analyse the changes in α, we isolate the polarization-dependent component of the photocurrent (V_{Lin}) by fitting a sinusoidal function (Fig. 2a) and subtracting the polarization-independent background. Figure 2b plots $V_{Lin}(\theta_p, \nu)$. The white lines mark the sign changes in the photoresponse, thereby tracking the changes in α. Strikingly, we find a strong change with ν. A drift in α is observed at the CNP (raw data are shown in Fig. 2a) and additional sharp drifts at around ν = −1 (Fig. 2c). Figure 2d plots α(ν) highlighting the winding of α at the CNP and integer ν. α stabilizes for intermediate ν and then drifts again, approaching ν = ±4. Prominent changes were also observed in D1.03 (Fig. 2e) and D1.12 (Fig. 2f) (Supplementary Section 2),

https://doi.org/10.1038/s41563-025-02180-3

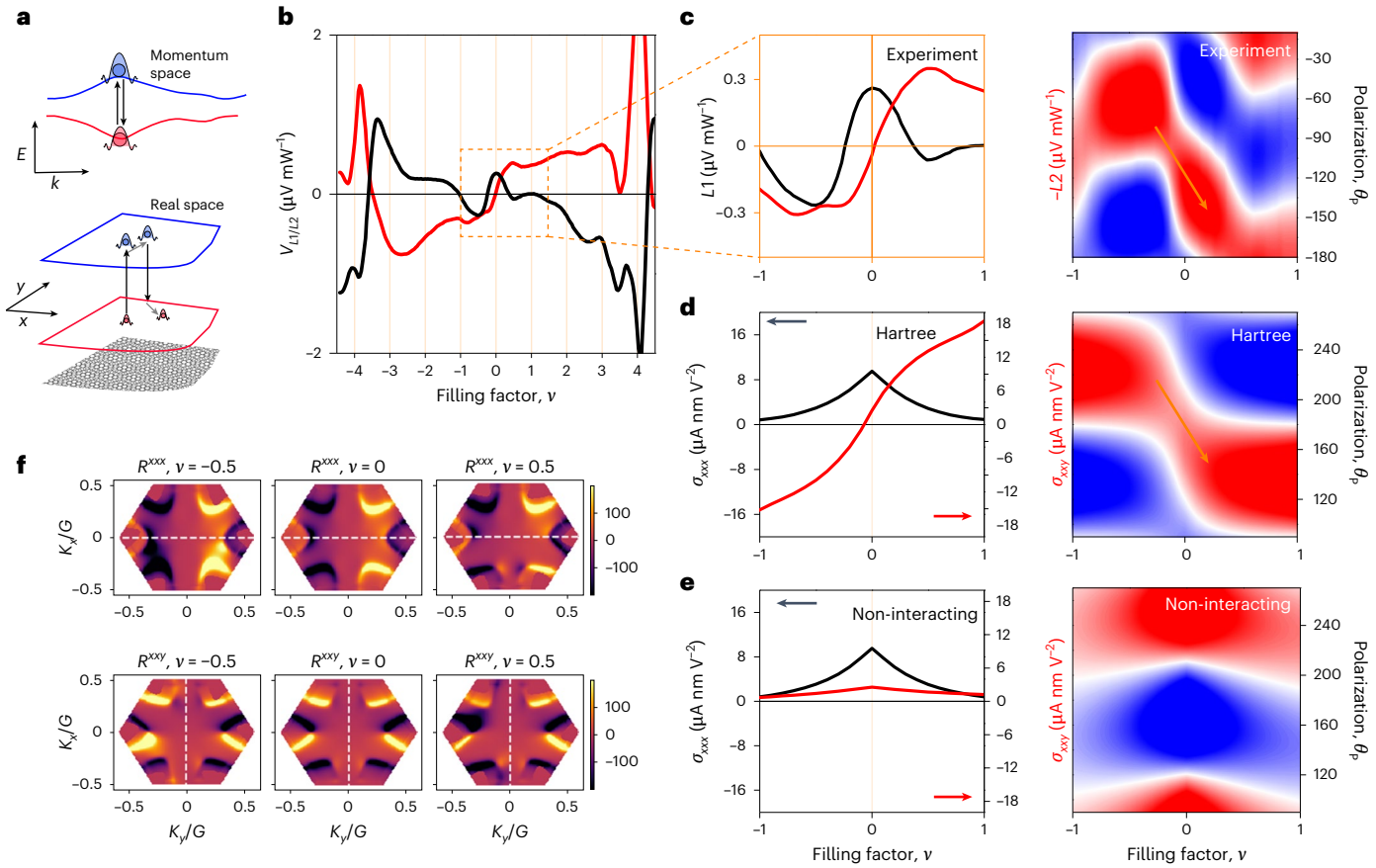

Fig. 3 | Hartree-interaction-induced THz photocurrents. a, Schematic illustrating shift currents. Top: illustration of interband transitions. Bottom: the real space corresponding to the manifolds of the valence (red) and conduction (blue) bands. Electrons experience real-space shifts of the wavepacket when transitioning between bands. **b**, Experimentally extracted $L1$ and $L2$ values as a function of ν in D0.94. **c**, Left: zoomed-in view of **b** close to the CNP. Right: zoomed-in view of Fig. 2b close to the CNP. **d**,**e**, Left: shift current conductivities as a function of ν at 6-meV excitation with (**d**) and without (**e**) Hartree interactions. σ_{xxx}, left axis (black); σ_{xxy}, right axis (red). Right: simulated photocurrent maps using the calculated $\sigma_{xxx}/\sigma_{xxy}$ values with (**d**) and without (**e**) Hartree interactions. The yellow arrows indicate the direction of α drift. Qualitatively similar behaviours are observed for different modelling parameters including wavelength, twist angle and hopping parameters (Supplementary Section 6). **f**, K-space plots of the shift vector integrand $R_{\alpha\beta c}$ for the two components of conductivity. Different columns and rows indicate different ν values and components, respectively. The dashed white line represents a high-symmetry axis for which we plot the case with and without Hartree interactions on either side of the hexagon.

although the specifics vary across different devices. This variation reflects subtle differences in the electronic structure and competing contributions to the measured photoresponse. Key features, particularly sharp drifts in α close to the CNP and $\nu = \pm 4$, were identified in all the studied devices. Moreover, features near integer ν appear as peaks/dips in α (Fig. 2d–f, red arrows) or sharp drifts in α (Fig. 2d,e, blue arrows), resembling the behaviour at the CNP.

Hartree-renormalized shift current response

The changes in α with ν provide strong evidence for its connection to the BPE[14,17]. In this case, the photoresponse is governed by second-order conductivities, $J_c = \sigma_{abc}E_aE_b, \{a,b,c\} = \{x,y\}$, where E_x and E_y describe the components of the electric field projected onto the principal vectors of the two-dimensional crystal lattice. We proceed to understand possible contributions and compare them with those extracted from our experiment by decomposing α into two principal vectors with amplitudes $L1$ and $L2$, according to $\alpha = \tan^{-1}(L1/L2)$. Therefore, the photoresponse can be described as

$$V_{PV} = L1\sin(2\theta) + L2\cos(2\theta) + D, \quad (1)$$

where D is a polarization-independent contribution. This signal decomposition is formally identical to that shown in Fig. 2d–f; however, it allows a more direct comparison between the conductivity tensor elements and the experimental coefficients (Supplementary Section 6). Specifically, for systems with C_3 symmetry, there exist two independent components, namely, $\sigma_{xxx}/\sigma_{xxy}$, which, up to a rotation of the reference frame, correspond to $L1/L2$ in equation (1). The extracted coefficients are plotted in Fig. 3b for D0.94, aligning the reference frame with the direction in which the CNP response is the maximum ($\theta_p \approx 45°$).

We must identify the microscopic mechanism of the photoresponse. We first focus on the behaviour around the CNP at which all the devices show photoresponse evolving from a sign-changing to a peaked response (Fig. 1f–h), alongside drifts in α (Fig. 2a,d–f). There are two possible contributions to the second-order conductivity: intraband and interband excitations. The former pertains to quantum nonlinear electrical responses[18,32,33]. However, measurements of the second-harmonic voltage—a typical signature of these Fermi surface effects—showed rather different behaviours, distinguishing its microscopic origin (Supplementary Section 7). Crucially, intraband effects could not explain the peaked response at the CNP. In the absence of a Fermi surface, this response is more characteristic of an interband transition[19,20]. As the photoresponse arises from linearly polarized light preserving time-reversal symmetry, we tentatively assign its origin to shift currents. These are second-order responses that arise from a real-space shift experienced by an electron wavefunction on an

https://doi.org/10.1038/s41563-025-02180-3

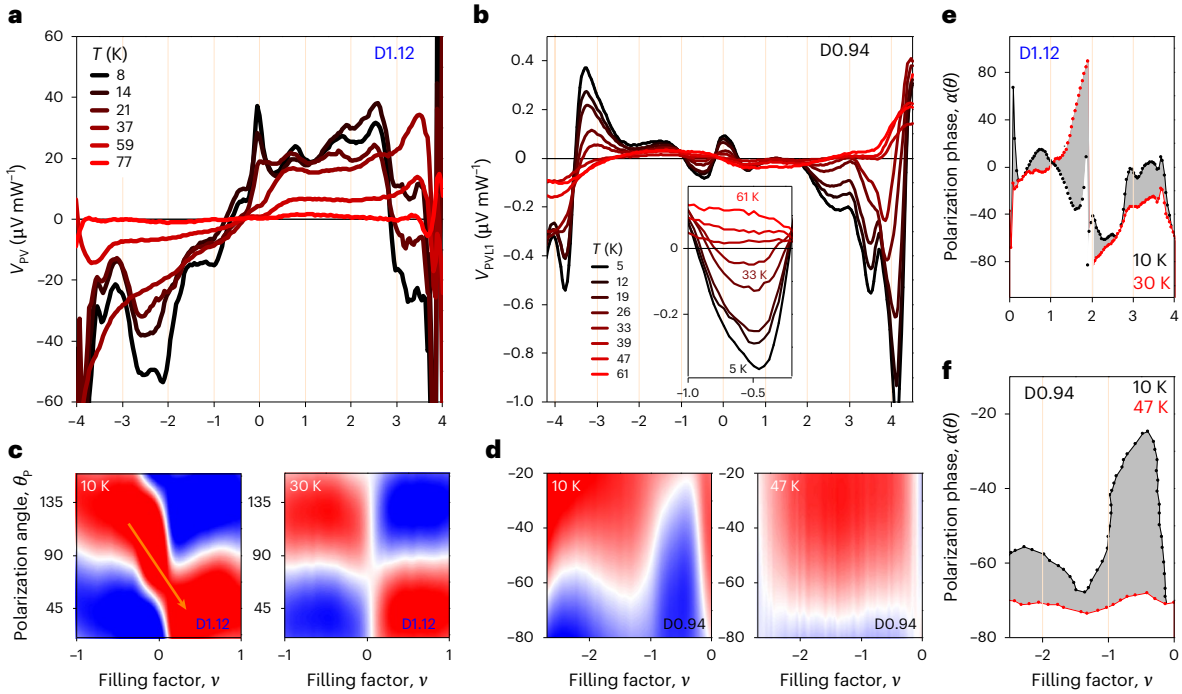

Fig. 4 | Temperature dependence of photoresponse and α. a, V_{PV} (μV mW^{-1}) as a function of ν for different temperatures from 8 K to 77 K in D1.12. **b**, Same as **a**, but for the linear component of the photovoltage V_{Lin_L1} (μV mW^{-1}) measured at different T values in D0.94. Inset: zoomed-in view around $\nu = 1$. **c**, V_{Lin} as a function of θ_P and ν measured in D1.12 at 10 K (left) and 30 K (right) zoomed around the CNP. Colour scale, blue (−50 μV mW^{-1}); red (50 μV mW^{-1}). **d**, Same data as **c**, but for D0.94 at 10 K (left) and 47 K (right) zoomed around integer ν. Colour scale, blue (−0.8 μV mW^{-1}); red (0.8 μV mW^{-1}). **e**,**f**, α measured as a function of ν for low and high temperatures in D1.12 (**e**) and D0.94 (**f**). The shaded areas highlight the differences in α.

interband excitation driven by linearly polarized light (Fig. 3a). These photocurrents were previously reported in moiré materials at infrared frequencies[17] and are expected to be amplified at THz frequencies at which they are more sensitive to flat-band physics.

To account for shift currents, we calculate σ_{xxx} and σ_{xxy} (Supplementary Section 6). Because our excitation energies are smaller than the flat, remote bandgaps (Supplementary Section 8), we consider only transitions between flat bands (Fig. 3a). Figure 3d,e shows these calculations for two scenarios: the non-interacting (Fig. 3d) and Hartree-renormalized (Fig. 3e) band structures[34], which accounts for the charge redistribution of the TBG system[34] and is expected to be the leading interaction effect above 10 K. Comparing calculations (Fig. 3d,e, left) with the measured $L1$ and $L2$ values (Fig. 3c, left), we find that our photoresponse is well described by the shift current conductivities only when considering Hartree interactions. Indeed, although the peaked response at the CNP ($L1$) is captured by both interacting and non-interacting σ_{xxx}, the sharp sign-changing response ($L2$) is unique to the Hartree σ_{xxy} value (Fig. 3e). This distinction is crucial, since it provides the exact ingredients to observe α drifts close to the CNP. This is observed in Fig. 3d,e (right), which plots the simulated photocurrent maps, showing that the α drift is unique to the interacting case.

Hartree interactions strongly modify the σ_{xxy} component and leave σ_{xxx} largely unaltered. This difference stems from the microscopic components of shift current, where different states in the moiré Brillouin zone contribute differently. Specifically, Hartree interactions strongly affect the states near the K/K′ points of the moiré Brillouin zone[34] (Fig. 3f), the regions that contribute to the σ_{xxy} component (Supplementary Section 6). The α drift through the CNP is attributed to the two distinct ν-dependent conductivities and, hence, serves as a photocurrent fingerprint of Hartree interactions in the TBG. Moreover, the prominent modifications around the CNP demonstrate that even minimal doping strongly distorts the quantum geometry of bands.

Broken-symmetry states

On the general grounds of symmetry analysis, the presence of shift currents in our devices implies that $C_{2z}T$ symmetry[35] must be broken and there should be a necessary gapping of flat bands[10] in all our devices. This is at odds with the fact that only D1.03 was explicitly aligned with hBN and exhibited an insulating state at the CNP, whereas D0.94 and D1.12 were metallic. These observations are in line with quantum transport experiments in which broken-$C_{2z}T$-symmetry phases were observed despite the absence of extrinsic symmetry-breaking factors[6,23] and point towards an underlying hidden symmetry. In particular, the insulating behaviour observed at the CNP in non-aligned devices has sparked considerable interest in the ground state[23,36,37], where several interaction-driven phases have been predicted. Furthermore, recent tight-binding calculations demonstrated that hBN has a non-negligible impact on TBG's electronic spectrum due to reconstruction effects and strain fields that break the sub-lattice symmetry even for alignment angles larger than 6° (refs. 38,39). Calculations of the bands for D0.94 and D1.12 indeed demonstrated that gaps of 3–4 meV emerge, caused by the alignment of hBN with graphene within 4° (Supplementary Sections 9 and 10). Since we observe polarization-dependent photocurrents for all ν, we believe that substrate effects play a major role. This is further supported by the observation of bulk photocurrents in TBG devices at non-magic angles (Supplementary Section 11), where interactions are less relevant, and measurements between different contact pairs allowed us to map out the C_3 symmetry of the system. Aside from the hBN substrate, we note that additional extrinsic symmetry-breaking factors may contribute, including local strain gradients that are known to generate strong BPEs[40].

To better understand the gapped state at the CNP and integer-ν features, we studied the temperature dependence of the photoresponse. Figure 4a,b plots the photovoltages measured in D1.12 and D0.94 for different temperatures. In both cases, the photoresponse decreases rapidly as T approaches 50 K. This is expected for an

https://doi.org/10.1038/s41563-025-02180-3

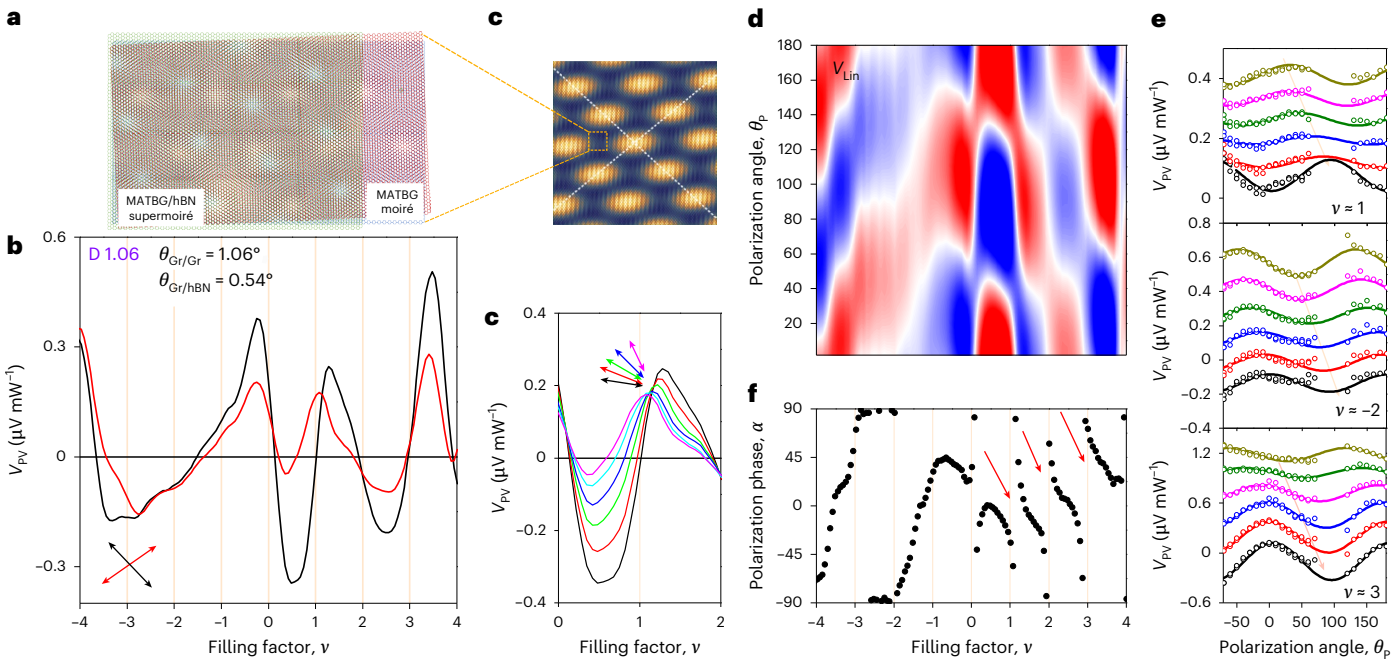

Fig. 5 | Photocurrent cascade in commensurate TBG aligned to hBN with a supermoiré potential. a, Schematic of TBG aligned to hBN for commensurate twist angles, where graphene–graphene and graphene–hBN superlattices bare similar periodicities resulting in a supermoiré structure. Right: a supermoiré lattice in the presence of weak strain (~0.1%) adapted from ref. 43. MATBG, magic-angle TBG. **b**, Photovoltage measurements made between a different contact pair in D1.03 for $\theta_p = 10°$ (black) and $\theta_p = 60°$ (red). Gr, graphene. **c**, Zoomed-in view of the data in **b**, close to $\nu = 1$. **d**, $V_{Lin}(\theta, \nu)$ for D1.03 with the same pair of contacts as in **b**. **e**, $V_{PV}(\theta)$ plotted for different ν values close to integer ν. The open circles are experimental data, whereas the solid lines are sinusoidal fits. **f**, α as a function of ν plotted in D1.03 The red arrows highlight drifts in α at integer ν observed in D1.03.

interband response, which is suppressed by the temperature smearing of the Fermi–Dirac distribution[19] when approaching the energy scale of the flat bands. However, the CNP response and integer-ν features disappear much faster at 30 K. Although the system still exhibits polarization dependence, the phase drifts at CNP (Fig. 4c) and integer ν (Fig. 4d) disappear. Figure 4e,f further highlights this through plots of $\alpha(\nu)$ for D1.12 and D0.94 for two temperatures. The complex temperature dependence in α, hence, suggests an interplay of symmetry breaking induced by both extrinsic factors (hBN substrate/strain gradients) and intrinsic factors (interaction effects).

Our measurements demonstrate that the photocurrent is more sensitive to probing gapped states than quantum transport[13]. This is because the latter requires well-defined gapped regions on mesoscopic length scales, which are easily shunted by edges[41] or domains[42]. Bulk photocurrent measurements, however, are not sensitive to ungapped regions in the same way. The gapped regions generate the photoresponse and the ungapped regions serve only as current-collecting leads. Indeed, our measurements between different contact pairs show that α has a non-trivial dependence, probably reflecting spatial variations in local symmetry (Supplementary Section 12). Hence, the gap in our non-aligned devices is probably localized to a specific region[37], which would be undetectable in quantum transport measurements.

Cascade phenomena

In addition to the sharp α drifts at the CNP, we observed additional peaks/dips or drifts in α close to integer ν, which smear with temperature (Fig. 4). Figure 5b plots V_{PV} measured between different contact pairs in D1.03—the device in which signatures of alignment with hBN manifest in quantum transport and near-field measurements performed previously[43]. Interestingly, we find that the photoresponse is markedly different. Not only is the peaked response at the CNP suppressed but V_{PV} also exhibits strong oscillations changing sign close to integer ν. The former can be attributed to strain effects, which are amplified by second-order superlattices[43] (Supplementary Section 6). However, the oscillatory structure cannot be accounted for by a single-particle picture. In particular, with changing polarization, the behaviour around $\nu = 1$ resembles the behaviour at CNP observed in other devices, namely, a peaked response evolving smoothly from a sign-changing response (Fig. 5c). Moreover, the sign-changing response is accompanied by α drifts through all integer ν (Fig. 5d–f).

The α drifts, mirroring that at the CNP (Fig. 3c), reflect the behaviour intrinsic to the cascade of phase transitions[25,26,44] in magic-angle TBG, where the chemical potential resets repeatedly at integer filings. In this case, our photocurrent measurements shed light on several empirical observations. First, according to our model (Fig. 3), the α drifts suggest that these states may be gapped like the CNP. Second, the pronounced polarization dependence at $\nu = 1$ compared with other ν values (Fig. 5c) suggests that the symmetry of the underlying many-body ground states may vary across different ν values (refs. 45,46). This variation is attributed to the polarization dependence at $\nu = 1$, which requires two distinct and independent components of second-order conductivity, in contrast to $\nu = 2$ and $\nu = 3$. Third, the sign change in photoresponse at integer ν reveals that the electronic orders differ after reset, reflecting subtle changes in the wavefunctions. Adopting the Stoner-like interpretation of ref. 26, where the carriers preferentially occupy one of the four degenerate valleys and/or spin-polarized bands[26], our photocurrent measurements appear to track these phase transitions, with a sign change following each reset. Although the shift current is insensitive to valley polarization, the linear injection current is[13,14], suggesting that the oscillatory structure reflects the interplay of flavour polarization with the spontaneous breaking of time-reversal symmetry. Concurrently, recent low-temperature scanning tunnelling microscopy experiments have revealed the presence of intervalley coherent states at half-filling[37,47]. This observation, combined with our measurements, calls for a more profound exploration of how flat bands and their quantum geometry deform during cascade, for example,

through the heavy fermion model[48,49]. Finally, we note that cascade features could be observed in a fourth TBG sample without commensurate alignment to hBN, although with contributions from junction effects via the photothermoelectric effect (Supplementary Fig. 8), which seemingly dominates in the case of weaker C_{2z}-symmetry breaking.

Discussion

The observed changes in α with carrier doping underscores the BPE in moiré devices[17], whereas its occurrence in TBG without strict alignment to hBN suggests that the substrate plays a more subtle role in determining their symmetry and many-body phases. Although further work is required to understand the photoresponse at high ν and the details of the cascade features, our work demonstrates the sensitivity of photocurrent in probing hidden symmetry of the underlying ground state not easily probed via conventional transport measurements. The rising interest in the quantum metric tensor and its strong influence on the electromagnetic response has long called for a technique that is fast and accessible. The direct connection between second-order conductivities and the quantum geometry underlying the THz photocurrent response provides a fast and powerful tool in this direction, which may be leveraged to probe its interplay with strongly correlated phenomena[50]. The impact of strain should be further explored because of its known influence on the phase diagram of TBG and strong influence on second-order conductivities (Supplementary Section 6). Finally, although we observe dominating contributions from shift currents owing to the large moiré crystal unit cell, the role of ballistic currents[15] remains an intriguing topic for further studies.

From a technological perspective, the measured devices hold strong prospects for THz applications. We find extrinsic voltage responsivities of around 200 mV W^{-1}, which are large considering the device area is 1,000 times smaller than the illumination area, and project an intrinsic noise-equivalent power (NEP) of 10^{-12} W $Hz^{-0.5}$ (Supplementary Section 13). These metrics are competitive with previous low-temperature detectors[51], offering major advantages including facile scalability and extraordinary polarization sensitivity. Specifically, moiré materials can be engineered in multilayer configurations to enhance extrinsic absorption and preserve their desirable few-layer properties including a large THz quantum geometric response[52,53]. Moreover, the complex polarization and wavelength dependencies present exciting prospects for on-chip THz polarimetry applications[17].

Online content

Any methods, additional references, Nature Portfolio reporting summaries, source data, extended data, supplementary information, acknowledgements, peer review information; details of author contributions and competing interests; and statements of data and code availability are available at https://doi.org/10.1038/s41563-025-02180-3.

References

1. Cao, Y. et al. Unconventional superconductivity in magic-angle graphene superlattices. *Nature* **556**, 43–50 (2018).
2. Cao, Y. et al. Correlated insulator behaviour at half-filling in magic-angle graphene superlattices. *Nature* **556**, 80–84 (2018).
3. Andrei, E. Y. & MacDonald, A. H. Graphene bilayers with a twist. *Nat. Mater.* **19**, 1265–1275 (2020).
4. Sharpe, A. L. et al. Emergent ferromagnetism near three-quarters filling in twisted bilayer graphene. *Science* **365**, 605–608 (2019).
5. Serlin, M. et al. Intrinsic quantized anomalous Hall effect in a moiré heterostructure. *Science* **367**, 900–903 (2020).
6. Stepanov, P. et al. Competing zero-field chern insulators in superconducting twisted bilayer graphene. *Phys. Rev. Lett.* **127**, 197701 (2021).
7. Andrei, E. Y. et al. The marvels of moiré materials. *Nat. Rev. Mater.* **6**, 201–206 (2021).
8. Tschirhart, C. L. et al. Imaging orbital ferromagnetism in a moiré Chern insulator. *Science* **372**, 1323–1327 (2021).
9. Grover, S. et al. Chern mosaic and Berry-curvature magnetism in magic-angle graphene. *Nat. Phys.* **18**, 885–892 (2022).
10. Cea, T., Pantaleón, P. A. & Guinea, F. Band structure of twisted bilayer graphene on hexagonal boron nitride. *Phys. Rev. B* **102**, 155136 (2020).
11. Kazmierczak, N. P. et al. Strain fields in twisted bilayer graphene. *Nat. Mater.* **20**, 956–963 (2021).
12. Carr, S., Fang, S., Zhu, Z. & Kaxiras, E. Exact continuum model for low-energy electronic states of twisted bilayer graphene. *Phys. Rev. Res.* **1**, 13001 (2019).
13. Ma, Q., Krishna Kumar, R., Xu, S.-Y., Koppens, F. H. L. & Song, J. C. W. Photocurrent as a multiphysics diagnostic of quantum materials. *Nat. Rev. Phys.* **5**, 170–184 (2023).
14. Ma, Q., Grushin, A. G. & Burch, K. S. Topology and geometry under the nonlinear electromagnetic spotlight. *Nat. Mater.* **20**, 1601–1614 (2021).
15. Dai, Z. & Rappe, A. M. Recent progress in the theory of bulk photovoltaic effect. *Chem. Phys. Rev.* **4**, 11303 (2023).
16. Nakamura, M. et al. Shift current photovoltaic effect in a ferroelectric charge-transfer complex. *Nat. Commun.* **8**, 281 (2017).
17. Ma, C. et al. Intelligent infrared sensing enabled by tunable moiré quantum geometry. *Nature* **604**, 266–272 (2022).
18. Duan, J. et al. Giant second-order nonlinear Hall effect in twisted bilayer graphene. *Phys. Rev. Lett.* **129**, 186801 (2022).
19. Chaudhary, S., Lewandowski, C. & Refael, G. Shift-current response as a probe of quantum geometry and electron-electron interactions in twisted bilayer graphene. *Phys. Rev. Res.* **4**, 013164 (2022).
20. Kaplan, D., Holder, T. & Yan, B. Twisted photovoltaics at terahertz frequencies from momentum shift current. *Phys. Rev. Res.* **4**, 013209 (2022).
21. Arora, A., Kong, J. F. & Song, J. C. W. Strain-induced large injection current in twisted bilayer graphene. *Phys. Rev. B* **104**, L241404 (2021).
22. Pantaleón, P. A., Low, T. & Guinea, F. Tunable large Berry dipole in strained twisted bilayer graphene. *Phys. Rev. B* **103**, 205403 (2021).
23. Lu, X. et al. Superconductors, orbital magnets and correlated states in magic-angle bilayer graphene. *Nature* **574**, 653–657 (2019).
24. Xie, Y. et al. Spectroscopic signatures of many-body correlations in magic-angle twisted bilayer graphene. *Nature* **572**, 101–105 (2019).
25. Wong, D. et al. Cascade of electronic transitions in magic-angle twisted bilayer graphene. *Nature* **582**, 198–202 (2020).
26. Zondiner, U. et al. Cascade of phase transitions and Dirac revivals in magic-angle graphene. *Nature* **582**, 203–208 (2020).
27. Li, G. et al. Infrared spectroscopy for diagnosing superlattice minibands in twisted bilayer graphene near the magic angle. *Nano Lett.* **24**, 15956–15963 (2024).
28. Xu, X., Gabor, N. M., Alden, J. S., van der Zande, A. M. & McEuen, P. L. Photo-thermoelectric effect at a graphene interface junction. *Nano Lett.* **10**, 562–566 (2010).
29. Candussio, S. et al. Edge photocurrent driven by terahertz electric field in bilayer graphene. *Phys. Rev. B* **102**, 45406 (2020).
30. Castilla, S. et al. Fast and sensitive terahertz detection using an antenna-integrated graphene pn junction. *Nano Lett.* **19**, 2765–2773 (2019).
31. Semkin, V. A. et al. Zero-bias photodetection in 2D materials via geometric design of contacts. *Nano Lett.* **23**, 5250–5256 (2023).
32. Sinha, S. et al. Berry curvature dipole senses topological transition in a moiré superlattice. *Nat. Phys.* **18**, 765–770 (2022).

33. He, P. et al. Graphene moiré superlattices with giant quantum nonlinearity of chiral Bloch electrons. *Nat. Nanotechnol.* **17**, 378–383 (2022).
34. Guinea, F. & Walet, N. R. Electrostatic effects, band distortions, and superconductivity in twisted graphene bilayers. *Proc. Natl Acad. Sci. USA* **115**, 13174–13179 (2018).
35. Ma, C. et al. Moiré band topology in twisted bilayer graphene. *Nano Lett.* **20**, 6076–6083 (2020).
36. Jiang, Y. et al. Charge order and broken rotational symmetry in magic-angle twisted bilayer graphene. *Nature* **573**, 91–95 (2019).
37. Nuckolls, K. P. et al. Quantum textures of the many-body wavefunctions in magic-angle graphene. *Nature* **620**, 525–532 (2023).
38. Long, M. et al. An atomistic approach for the structural and electronic properties of twisted bilayer graphene-boron nitride heterostructures. *npj Comput. Mater.* **8**, 73 (2022).
39. Song, J. C. W., Shytov, A. V. & Levitov, L. S. Electron interactions and gap opening in graphene superlattices. *Phys. Rev. Lett.* **111**, 266801 (2013).
40. Jiang, J. et al. Flexo-photovoltaic effect in MoS_2. *Nat. Nanotechnol.* **16**, 894–901 (2021).
41. Zhu, M. J. et al. Edge currents shunt the insulating bulk in gapped graphene. *Nat. Commun.* **8**, 14552 (2017).
42. Uri, A. et al. Mapping the twist-angle disorder and Landau levels in magic-angle graphene. *Nature* **581**, 47–52 (2020).
43. Hesp, N. C. H. et al. Cryogenic nano-imaging of second-order moiré superlattices. *Nat. Mater.* **23**, 1664–1670 (2024).
44. Choi, Y. et al. Correlation-driven topological phases in magic-angle twisted bilayer graphene. *Nature* **589**, 536–541 (2021).
45. Kwan, Y. H. et al. Kekulé spiral order at all nonzero integer fillings in twisted bilayer graphene. *Phys. Rev. X* **11**, 41063 (2021).
46. Lian, B. et al. Twisted bilayer graphene. IV. Exact insulator ground states and phase diagram. *Phys. Rev. B* **103**, 205414 (2021).
47. Kim, H. et al. Imaging inter-valley coherent order in magic-angle twisted trilayer graphene. *Nature* **623**, 942–948 (2023).
48. Song, Z.-D. & Bernevig, B. A. Magic-angle twisted bilayer graphene as a topological heavy fermion problem. *Phys. Rev. Lett.* **129**, 47601 (2022).
49. Datta, A., Calderón, M. J., Camjayi, A. & Bascones, E. Heavy quasiparticles and cascades without symmetry breaking in twisted bilayer graphene. *Nat. Commun.* **14**, 5036 (2023).
50. Tian, H. et al. Evidence for Dirac flat band superconductivity enabled by quantum geometry. *Nature* **614**, 440–444 (2023).
51. Bandurin, D. A. et al. Resonant terahertz detection using graphene plasmons. *Nat. Commun.* **9**, 5392 (2018).
52. Khalaf, E., Kruchkov, A. J., Tarnopolsky, G. & Vishwanath, A. Magic angle hierarchy in twisted graphene multilayers. *Phys. Rev. B* **100**, 085109 (2019).
53. Park, J. M. et al. Robust superconductivity in magic-angle multilayer graphene family. *Nat. Mater.* **21**, 877–883 (2022).

[1]ICFO—Institut de Ciencies Fotoniques, The Barcelona Institute of Science and Technology, Castelldefels (Barcelona), Spain. [2]Catalan Institute of Nanoscience and Nanotechnology (ICN2), CSIC and The Barcelona Institute of Science and Technology (BIST), Campus UAB, Bellaterra, Spain. [3]Department of Physics, The University of Texas, Austin, TX, USA. [4]Department of Physics, Massachusetts Institute of Technology, Cambridge, MA, USA. [5]IMDEA Nanociencia, Madrid, Spain. [6]JARA-FIT and 2nd Institute of Physics, RWTH Aachen University, Aachen, Germany. [7]Peter Grünberg Institute (PGI-9), Forschungszentrum Jülich, Jülich, Germany. [8]Université Côte d'Azur, CNRS, CRHEA, Sophia-Antipolis, France. [9]Research Center for Materials Nanoarchitectonics, National Institute for Materials Science, Tsukuba, Japan. [10]Research Center for Electronic and Optical Materials, National Institute for Materials Science, Tsukuba, Japan. [11]Department of Physics and Institute for Quantum Information and Matter, California Institute of Technology, Pasadena, CA, USA. [12]Donostia International Physics Center, San Sebastian, Spain. [13]Division of Physics and Applied Physics, School of Physical and Mathematical Sciences, Nanyang Technological University, Singapore, Singapore. [14]Department of Physics and Astronomy, University of Notre Dame, Notre Dame, IN, USA. [15]Stavropoulos Center for Complex Quantum Matter, University of Notre Dame, Notre Dame, IN, USA. [16]National High Magnetic Field Laboratory, Tallahassee, FL, USA. [17]Department of Physics, Florida State University, Tallahassee, FL, USA. [18]ICREA—Institució Catalana de Recerca i Estudis Avançats, Barcelona, Spain. [19]These authors contributed equally: Geng Li, Riccardo Bertini, Swati Chaudhary. ✉e-mail: roshan.krishnakumar@icfo.eu; frank.koppens@icfo.eu

Methods

Device fabrication

Our devices (Supplementary Fig. 1) were fabricated using standard methods in two-dimensional material fabrication[54]. For TBG, the heterostructures were assembled using the 'cut-and-stack' method[55]. In all devices, graphite gates were incorporated into the heterostructures to allow for pristine electrical gating. Following heterostructure assembly, nanolithography was performed on the mesa and gold leads to electrically contact the channel. In D0.94, D1.12, D1.5 and D1.03, selective etching (SF_6 and O_2) was used to expose the graphene channel without etching through the gate. Subsequent deposition of Cr/Au (5/60 nm thick) was made via electron-beam and thermal evaporation processes, respectively. This method ensures that the entire active channel is gate tunable and removes possible junctions that can arise due to graphite gates (Supplementary Section 5). In D1.02 and bilayer graphene/monolayer graphene devices, the device was contacted in regions extending outside of the graphite gates. Finally, we note that some devices were fabricated on low-doped Si/SiO_2 (285 nm) substrates (D0.94, D1.12, D1.02, D1.5 and monolayer graphene) and others on highly doped Si/SiO_2 (285 nm) substrates (bilayer graphene devices and D1.03). These differences may result in different extrinsic absorptions of THz radiation depending on the choice of substrate.

Cryogenic photocurrent and electrical measurements

Quantum transport and THz photocurrent measurements were performed on an Advanced Research System 4-K cryostat with optical access and temperature control. Electrical measurements were performed using standard a.c. lock-in techniques (Stanford) in combination with d.c. voltage sources (Keithley) for electrically gating our devices. Hall effect measurements were performed in the same cryostat using an electromagnet at 0.7 T. Independently, the cryostat could be raised out of the magnet and placed in the path for optical coupling. For THz illumination, a gas laser (Edinburgh Instruments) was used and focused into the cryostat using a lens on a cage system with a focal length of 20 mm. To rotate the polarization, we used polarizers (Purewave) in combination with quarter-wave plates (Tydex). The quarter-wave plate rotates the incident beam of polarization, allowing the arbitrarily selection of a polarization direction with the polarizer placed subsequently. In some cases, only a single polarizer was used to rotate the polarization. We verified that the photoresponse was linear with power, ensuring that normalizing by the incident power reflects the polarization dependence of the system. We also checked that performing polarization dependence measurements with a single polarizer, or with a wave-plate/polarizer geometry revealed identical results despite the latter enabling larger illumination powers. Experimental data were taken by fixing the polarization dependence and sweeping the gate voltage. Before and after each measurement, the power was measured using a room-temperature bolometer coupled via a flip mirror placed in the optical path.

Photodetector performance estimates

Because of the long wavelength intrinsic to THz radiation, our devices ($\sim 10 \times 30\ \mu m^2$) are much smaller than the focused THz beam ($120 < \lambda < 430\ \mu m$). Consequently, a large portion of the incident radiation is not absorbed. Hence, normalizing the photovoltage by the measured power at the room-temperature bolometer (Methods) is not representative of the inherent responsivity of our devices. To estimate the capabilities of our TBG devices for THz detection, we project the possible NEP values that may be obtainable in optimized devices with antenna integration. For this, we estimate the total power incident on the sample by calculating the fraction of the incident THz beam that is occupied by the device. Considering the wavelength at 0.7 THz (that is, 430 μm) and a numerical aperture of 0.12, the diffraction-limited beam-spot diameter is estimated to be 1.8 mm. Given that our devices are, at most, $10 \times 30\ \mu m^2$ in size, we find the device area ($3 \times 10^{-10}\ m^2$) to be around 8,000 times smaller than the area of the focused Gaussian beam ($2.5 \times 10^{-6}\ m^2$). Hence, the power axis (Supplementary Fig. 16) is normalized by this factor of 8,000 to estimate the potential responsivities and NEP values obtainable, for example, in a device with integrated antennas or if the device active area was upscaled. Because the device operates under a zero-bias voltage, we attribute the intrinsic noise floor to Johnson noise, with $R = 10{,}000\ \Omega$ (two-probe resistance of our devices), $T = 10$ K and 1 Hz. Extrapolating from Supplementary Fig. 16, we find NEP $= 7 \times 10^{-13}\ W\ Hz^{-0.5}$. The power-dependent measurements (Supplementary Fig. 16) were performed for $\theta_p = 50°$ illumination.

Data availability

The data that support the plots within this paper are available via Zenodo at https://doi.org/10.5281/zenodo.14882592 (ref. 56). Additional data including those from the Supplementary Information are available from the corresponding authors upon request.

References

54. Purdie, D. G. et al. Cleaning interfaces in layered materials heterostructures. *Nat. Commun.* **9**, 5387 (2018).
55. Cao, Y. et al. Superlattice-induced insulating states and valley-protected orbits in twisted bilayer graphene. *Phys. Rev. Lett.* **117**, 116804 (2016).
56. Krishna Kumar, R. Data for main text figs—terahertz photocurrent probe of quantum geometry and interactions in magic-angle twisted bilayer graphene. *Zenodo* https://doi.org/10.5281/zenodo.14882592 (2025).

Acknowledgements

R.B. acknowledges funding from the European Union's Horizon 2020 research and innovation programme under the Marie Skłodowska-Curie grant agreement no. 847517. J.B. acknowledges support from the European Union's Horizon Europe programme under grant agreement no. 101105218. K.N. acknowledges funding from the European Union's Horizon 2020 research and innovation programme under the Marie Skłodowska-Curie grant agreement no. 713729. S.C. acknowledges funding by the Departament de Recerca i Universitats de la Generalitat de Catalunya (no. 2021 SGR 01443). E.K. acknowledges funding under the Marie Skłodowska-Curie Fellowship project SuperTera. IMDEA Nanociencia acknowledges support from the 'Severo Ochoa' Programme for Centres of Excellence in R&D (no. CEX2020-001039-S/AEI/10.13039/501100011033). P.A.P. and F.G. acknowledge funding from the European Commission, within the Graphene Flagship Core 3 via grant no. 881603 and from grant no. NMAT2D (Comunidad de Madrid, Spain), SprQuMat, from NOVMOMAT, project PID2022-142162NB-I00 funded by MICIU/AEI/10.13039/501100011033 and by FEDER, UE, as well as financial support through the (MAD2D-CM)-MRR MATERIALES AVANZADOS-IMDEA-NC. Z.Z. acknowledges support from the European Union's Horizon 2020 research and innovation programme under the Marie Skłodowska-Curie grant agreement no. 101034431. S.B.-P. acknowledges support from the 'Presencia de la Agencia Estatal de Investigación' within the 'Convocatoria de tramitación anticipada, correspondente al año 2020, de las ayudas para contractos predoctorales (ref. no. PRE2020-094404) para la formación de doctores contemplada en el Subprograma Estatal de Fromación del Programa Estatal de Promoción del Talento y su Empleabilidad en I+D+i, en el marco del Plan Estatal de Investigacón Científica y Técnica de Innovación 2017–2020, cofinanciado por el Fondo Social Europeo'. E.I. and C.S. acknowledge funding from the European Union's Horizon 2020 research and innovation programme under grant agreement no. 881603 (Graphene Flagship) and from the European Research Council (ERC) under grant agreement no. 820254, the Deutsche Forschungsgemeinschaft (DFG, German Research Foundation) under Germany's Excellence Strategy—Cluster

of Excellence Matter and Light for Quantum Computing (ML4Q) EXC 2004/1–390534769 and the FLAG-ERA grant PhotoTBG–471733165. H.A. acknowledges funding from the European Union's Horizon 2020 research and innovation programme under Marie Skłodowska-Curie grant agreement no. 665884. K.W. and T.T. acknowledge support from JSPS KAKENHI (grant nos. 20H00354 and 23H02052) and World Premier International Research Center Initiative (WPI), MEXT, Japan. J.C.W.S. acknowledges support from the Singapore Ministry of Education under its Academic Research Fund Tier 2 grant no. MOE-T2EP50222-0011 and Tier 3 grant no. MOE-MOET32023-0003 Quantum Geometric Advantage. G.R. acknowledges support from the Simons Foundation, the ARO MURI grant no. W911NF-16-1-0361 and the Institute of Quantum Information and Matter. C.L. was supported by start-up funds from the Florida State University and the National High Magnetic Field Laboratory. The National High Magnetic Field Laboratory is supported by the National Science Foundation through NSF/DMR-2128556 and the State of Florida. P.J.-H. acknowledges support from the National Science Foundation (no. DMR-1809802), the STC Center for Integrated Quantum Materials (NSF grant no. DMR1231319), the Gordon and Betty Moore Foundation's EPiQS Initiative through grant no. GBMF9463, the Ramon Areces Foundation and the ICFO Distinguished Visiting Professor program. P.J.-H. acknowledges funding for his sabbatical by CEX2019-000910-S [MCIN/AEI/10.13039/501100011033] Fundacio Cellex, Fundacio Mir-Puig, and Generalitat de Catalunya through CERCA. This material is based on work supported by the Air Force Office of Scientific Research under award no. FA8655-23-17047. Any opinions findings, and conclusions or recommendations expressed in this material are those of the author(s) and do not necessarily reflect the views of the United States Air Force. F.H.L.K. acknowledges support from the ERC TOPONANOP under grant agreement no. 726001, the Gordon and Betty Moore Foundation through grant no. GBMF12212 and the Government of Spain (nos. FIS2016-81044; PID2019-106875GB-100; and Severo Ochoa CEX2019-000910-S [MCIN/AEI/10.13039/501100011033], PCI2021-122020-2A and PDC2022-133844-100 funded by MCIN/AEI/10.13039/501100011033). This work was also supported by the European Union NextGenerationEU/PRTR (PRTR-C17.I1) and EXQIRAL 101131579, Fundació Cellex, Fundació Mir-Puig and Generalitat de Catalunya (CERCA, AGAUR, 2021 SGR 014431656). Views and opinions expressed are those of the author(s) only and do not necessarily reflect those of the European Union Research Executive Agency. Neither the European Union nor the granting authority can be held responsible for them. Additionally, the research leading to these results received funding from European Union's Horizon 2020 programme under grant agreement nos. 881603 (Graphene Flagship Core 3) and 820378 (Quantum Flagship). This material is based on work supported by the Air Force Office of Scientific Research under award no. FA8655-23-1-7047. R.K.K. acknowledges funding by MCIN/AEI/10.13039/501100011033 and by the 'European Union NextGenerationEU/PRTR' PCI2021-122020-2A within the FLAG-ERA grant (PhotoTBG), by ICFO, RWTH Aachen and ETHZ/Department of Physics, and support from the Ramon y Cajal grant no. RYC2022-036118-I funded by MICIU/AEI/10.13039/501100011033 and by 'ESF+'.

Author contributions

R.K.K., K.N. and F.H.L.K. conceived the experiments. R.K.K. and R.B. performed the photocurrent measurements and analysed the data with support from K.N. G.L. fabricated the D0.94, D1.12 and D1.5 devices, and performed quantum transport measurements in these devices. P.S. fabricated the D1.03 device. S.C. performed the calculations and provided theoretical support regarding the shift current. J.M.P. fabricated the D1.02 device supported by P.J.-H. S.C. performed the numerical simulations. Z.Z. and P.A.P. performed the tight-binding calculations of TBG on hBN with support from F.G. R.K.K., R.B., H.A. and A.R.-P. built the cryogenic THz photocurrent setup in which the measurements were performed. S.B.-P. and J.B. performed the supporting photocurrent measurements. M.C. provided the fabrication support and technical expertise. E.I. fabricated the bilayer graphene devices supported by C.S. G.P. fabricated the monolayer graphene devices. E.K. provided technical assistance with the THz measurements. T.T. and K.W. provided the high-quality hBN crystals. G.R. provided theoretical support. J.C.W.S., C.L. and F.H.L.K. supervised the project. R.K.K., R.B., C.L. and F.H.L.K. wrote the manuscript with input from all authors.

Competing interests

The authors declare no competing interests.

Additional information

Supplementary information The online version contains supplementary material available at https://doi.org/10.1038/s41563-025-02180-3.

Correspondence and requests for materials should be addressed to Roshan Krishna Kumar or Frank H. L. Koppens.

Peer review information *Nature Materials* thanks Fan Zhang and the other, anonymous, reviewer(s) for their contribution to the peer review of this work.